JOURNAL OF SPACECRAFT AND ROCKETS
Vol. 33, No. 2, March–April 1996

Flap Efficiency and Heating of a Winged Re-Entry Vehicle

J. M. A. Longo* and R. Radespiel†
DLR, German Aerospace Research Establishment, D-38108 Braunschweig, Germany

Navier–Stokes solutions are analyzed for a winged re-entry vehicle at hypersonic freestream conditions corresponding to cold wing-tunnel tests and a flight trajectory point. The flow was assumed laminar and calorically perfect for the wind-tunnel case and in thermochemical equilibrium for the flight trajectory point. Computations are presented for clean configurations and for configurations with deflected control surfaces. The accuracy of the computed solutions is addressed by grid refinement studies and by comparing numerical results with available experimental data. Euler results are used to show the importance of the viscous effects on control surface efficiency. The impact of elevon camber on control efficiency and aerodynamic heating is also addressed. Strong changes in flow topology are found by changing from wind tunnel to flight conditions, in that local flow separations are reduced or suppressed. Additionally, significant three-dimensional effects on control surface heating are observed at flight conditions. However, only small losses of flap efficiency are found because of viscous effects.

Nomenclature

A	= attachment line
C_m	= pitching moment coefficient
H	= altitude
L	= reference length for pitching moment calculations; see Fig. 2
M	= Mach number
Re	= Reynolds number
S	= separation line
St	= Stanton number
St_{Mi}	= Stanton–Miller number
T	= temperature
t	= time
X, Y, Z	= body-fixed coordinate system
α	= angle of attack
γ	= ratio of specific heats of the gas mixture
ΔC_m	= control surface efficiency on pitching moment, $(C_{m,\delta\neq 0} - C_{m,\delta=0})$
δ	= deflection angle of the control surfaces
ρ	= density

Subscripts

w	= wall conditions
1	= primary
2	= secondary
∞	= freestream conditions

Introduction

THE aerodynamic design of winged re-entry vehicles (RV) is a severe engineering challenge because of the broad range of flow conditions present during the trajectory. A typical example is the European RV Hermes. By design, it is completely located within the forebody bow shock. The flight envelope for Hermes during re-entry comprises different aerodynamic domains[1] that reach from rarefied gas to subsonic flow (Fig. 1). Along its re-entry trajectory, the longitudinal and lateral control of the Hermes vehicle will be achieved by a combination of a reaction control system (RCS) and the use of aerodynamic surfaces. The initial entry phase extends to an attitude of approximately 75 km and an angle of attack of about 50 deg, during which the longitudinal control provided by the RCS will blend with the surface controls, the latter gaining in effectiveness as the dynamic pressure increases. The aerodynamic control surfaces of Hermes are cambered elevons, winglets with rudders, and a plane body flap, located at the lower aft end of the fuselage (Fig. 2). To maintain acceptable structural temperatures under entry heating environment, the maximum deflection angle of these control surfaces are restricted.

Flow simulations during the aerodynamic design should match not only flight Reynolds number and Mach number but also the thermochemical processes in the flow. Since that is not possible with present wind-tunnel technology, strong penalties should be introduced during design resulting from the large uncertainties in the extrapolation of wind-tunnel data to free flight. As an example one should recall that during the first entry of the U.S. Space Shuttle Orbiter, the vehicle had a larger nose-up pitching moment than predicted before flight that caused the longitudinal control surface to deflect twice the amount thought necessary to achieve trimmed flight.[2] Because of the increased sophistication and robustness of numerical flow solvers and a several order of magnitude increase in computer power, three-dimensional numerical simulations of hypersonic flow around complex configurations can now be used as transfer models.[3,4] The typical approach is to assume that once wind-tunnel flows obtained in cold or hot facilities can be reproduced with computational tools, the extrapolation to free-flight conditions will be similarly successful.

In the present paper, the efficiency of the longitudinal control surfaces of the Hermes spaceplane and the aerodynamic heating due to deflection are analyzed. The computed flowfields are obtained with the Navier–Stokes code CEVCATS.[5] The solutions are obtained for freestream conditions corresponding to cold wind-tunnel tests at $M_\infty = 10$ and a flight trajectory point at an altitude $H = 75$ km and $M_\infty = 25$. For the low-Mach number case, the flow is computed as laminar calorically perfect gas; for the high-Mach number case air

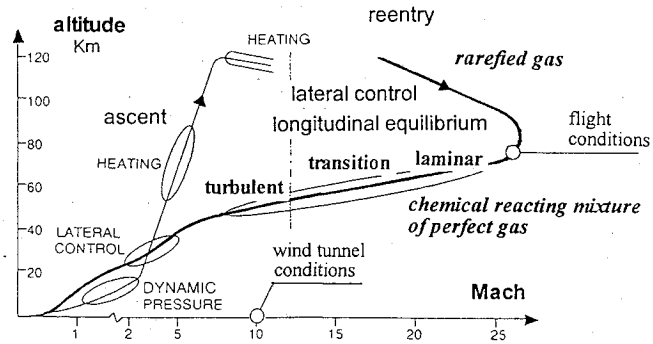

Fig. 1 Flight envelope for Hermes.[1]

Received Feb. 28, 1995; revision received Oct. 10, 1995; accepted for publication Oct. 13, 1995.

*Research Engineer, Aerothermodynamics Branch, Institute of Design Aerodynamics, Lilienthalplatz 7. Member AIAA.

†Head, Aerothermodynamics Branch, Institute of Design Aerodynamics, Lilienthalplatz 7. Member AIAA.

Table 1 Computed test cases

Case	Elevon	M_∞	α, deg	δ, deg	T_∞, K	T_w, K	Re	H, km	Gas
I	cambered	10	30	——	52	293	2.1×10^6	——	perfect
II	cambered	10	30	10	52	293	2.1×10^6	——	perfect
III	cambered	25	30	——	203	1300	3.5×10^5	75	equilib.
IV	cambered	25	30	10	203	1300	3.5×10^5	75	equilib.
V	plane	10	30	——	52	293	2.1×10^6	——	perfect
VI	plane	10	30	10	52	293	2.1×10^6	——	perfect
VII	plane	25	30	——	203	1300	3.5×10^5	75	equilib.
VIII	plane	25	30	10	203	1300	3.5×10^5	75	equilib.

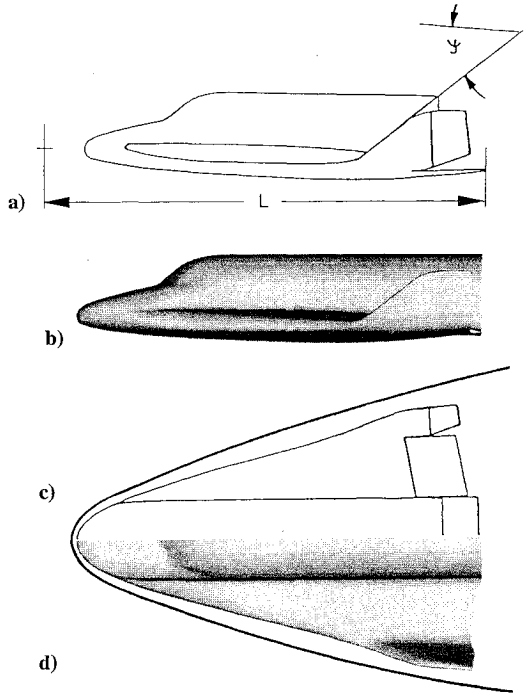

Fig. 2 Hermes configuration 1.0: a and c) measured and b and d) computed.

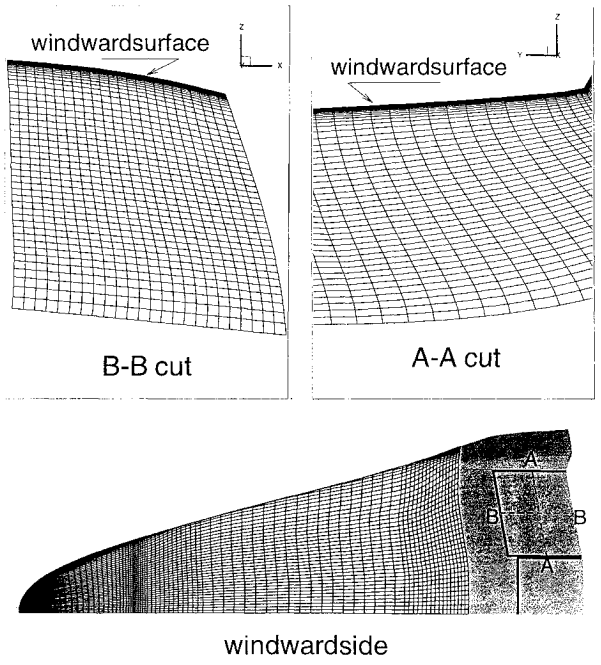

Fig. 3 Surface grid showing selected part of the configuration for control surface studies (shedding area) and field grid details near the elevon surface.

in thermochemical equilibrium is assumed. Computations are carried out for cambered and plane elevon geometries with and without body flap and elevons deflected. Table 1 summarizes the computed test cases. The accuracy of the numerical solutions is addressed by grid refinement studies and by comparing numerical results with available experimental data.[6,7] Also, previous Euler solutions[8] are used to show the importance of the viscous effects on pitching moment.

Numerical Simulation

Configuration and Grids

The geometry used for the present study corresponds to the shape 1.0 of the European spaceplane Hermes with some simplifications at the rear. Figure 2 compares the Hermes geometry with the surface definition adopted for the numerical simulation. The complex geometry of the Hermes at the body end results from the fact that the wing trailing edge extends farther downstream than the fuselage. In the present computational model the fuselage geometry is extended in axial direction up to the trailing edge of the root chord of the wing, which removes most of the upper surface of the body flap. Moreover, the slots between the control surfaces are closed, and the downstream boundary of the computational domain is defined at the end of the fuselage and wing. In the evaluation of forces and moments acting on the vehicle, corrections to the computational values are applied that take into account the neglected areas and moment arms. Recent flow computations[9] including the slots between rudder and elevon confirm that to neglect the slots does not affect the flow structure on the windwardside of the elevon surface. Finally, only half of the configuration is used for the numerical simulations, as only symmetric flow cases are investigated.

The size of the surface mesh consists of 144 cells in the streamwise and 96 cells in the spanwise direction. The resulting three-dimensional field grid (herein designated as global grid) has a C–O topology and exhibits a polar singularity at the nose of the vehicle. It consists of 914,225 grid points, where 64 cells are used in normal direction to the body surface. To allow flow computations with a limited amount of core memory and to reduce the total computational effort, a multiblock decomposition of the domain is used in combination with a local solution strategy. For each flow condition, a solution for the clean configuration is first obtained on the global grid. Then, local solutions are used to resolve the flow around the configuration with a deflected elevon. Since the flow is supersonic along the windward side of the configuration, only a local portion of the computational domain needs to be recomputed to evaluate the effects of surface deflection on the flow around the windward side.[10] Note that the leeside flow over the deflected elevon is not computed with this approach. Figure 3 shows the portion of the lower surface, shaded in gray, that is defined for the local computations. It includes 48 cells in streamwise direction, 40 cells in spanwise direction, and 64 cells in direction normal to the wall. Some details of the near-wall field grid in planes normal to the elevon in crosswise and streamwise direction are also displayed in Fig. 3. Mesh skewness is reasonably small near the surfaces. The aspect ratios for the near-wall cells are in the order of 1000. The flow conditions at the inflow boundaries of the local grid were obtained by interpolation of the solutions obtained with the global grid.

Computational Method

The computer code CEVCATS used for the present investigation has been extensively validated for a broad range of flows conditions

and configurations. Only a brief description is given here; the complete numerical formulation and validation examples are found in Ref. 5. CEVCATS is a computer code for the solution of the Navier–Stokes equations in integral form, using the thin-shear-layer approximation. Perfect gas, as well as thermochemical equilibrium flows, can be computed. For perfect gas cases, the laminar viscosity is computed with the Sutherland's formula. The high-temperature effects on the thermodynamic and transport properties of air in thermochemical equilibrium are implemented via vectorizable curve fits that are based on Tannehill curves. Solid walls are treated adiabatic, with prescribed temperature or in radiation equilibrium.

The spatial discretization is done by means of a second-order accurate, finite volume scheme that is implemented with the flow variables stored at the vertices of the cells. The numerical scheme consists of a hybrid upwind flux vector splitting. In regions of strong flow expansions and/or strong shock waves the van Leer scheme is used. In smooth flow regions, i.e., boundary layers, the scheme according to Liou is used. Second-order accuracy is obtained by MUSCL extrapolation of the density, velocity components, pressure, and total enthalpy. The solution is advanced in time by means of a five-stage Runge–Kutta scheme. Local time stepping, implicit residual averaging, and full multigrid are used to accelerate the convergence process.

For the present study a four level full-multigrid V cycle strategy in combination with a Courant number equal to 5 was used. Typical computer time on a single processor Cray Y-MP machine to execute one multigrid cycle for one grid point is about 100 μs. Figure 4 displays typical convergence rates of the code. Converged solutions are assumed once the rms of the derivative $\partial\rho/\partial t$ is reduced by three orders of magnitude.

Grid Convergence and Accuracy

Grid convergence studies are performed using partial and complete grid refinements, i.e., the refinement is done either in one specific coordinate direction or in all directions. Figure 5 shows the effects of a complete grid refinement of the heat fluxes and the resulting streamlines at the windward side of the configuration for the test case I. Also the figure indicates the position of the available experimental data with full circles. As the grid is refined, the lines of constant Stanton number show local peaks of aerodynamic heating at both sides of the elevon, close to the trailing edge. The camber of the elevon causes flow divergence at the elevon sides that is seen in the near-wall streamlines of the coarse and fine grid solutions. Moreover, the flow on the fine grid is close to separation at the elevon trailing edge.

Figure 6 shows line plots of computed and measured heat fluxes in selected planes for test case I. The size chosen for the experimental symbols corresponds to the wind-tunnel data accuracy. Also, the figure displays the local surface contours. The comparison of the computed results leads to the following observations: at the external elevon plane, near the trailing edge, the numerical simulation may be still improved by further grid refinement. On the first part of the external plane, as well as for the other two planes, the coarse and

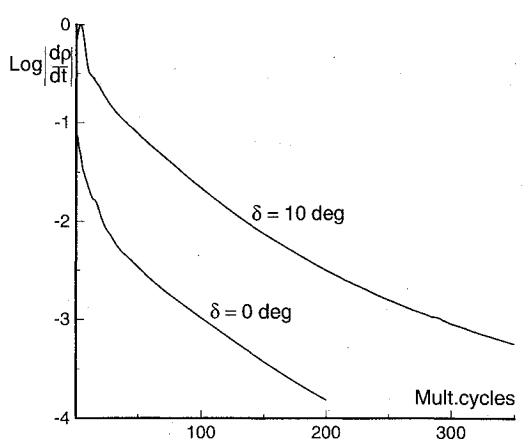

Fig. 4 History of convergence for cases VII and VIII.

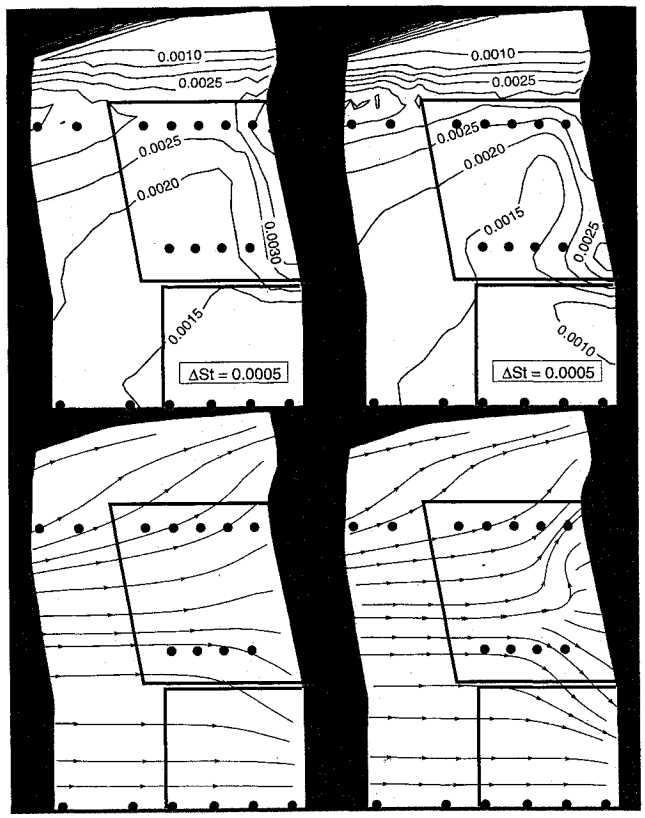

Fig. 5 Computed heat fluxes (top) and streamlines (bottom) for case I; grid sizes: left, 24 × 32 × 20 and right, 48 × 64 × 40.

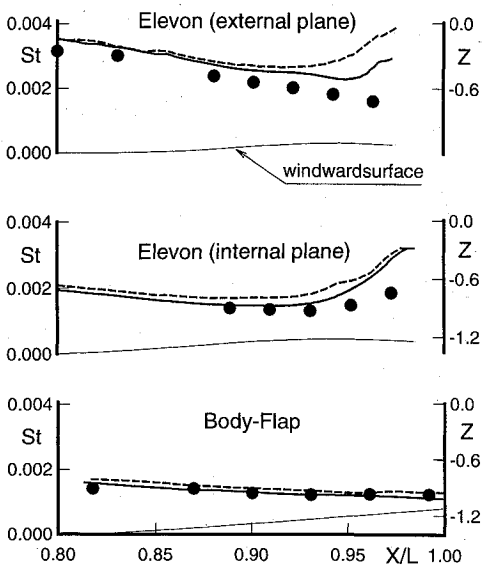

Fig. 6 Line plots of computed and measured Stanton number for case I: ——, fine grid; - - - -, coarse grid; and •, experiments.

fine grid solutions differ a little. There, the discrepancies between both solutions are of the order of the wind-tunnel accuracy. Although in an academic sense no grid independent solution is achieved for this test case, from a practical point of view a near grid-independent solution is provided for most of the control surface area. Note that the second-order scheme reduces the numerical errors by a factor of four if the grid spacing is halved in all coordinate directions. Hence, a new grid refinement will not result in significant changes except close to the trailing edge of the external plane. The comparison between numerical and experimental results indicates a good agreement. For the elevon, the agreement degrades as the trailing edge is approached. It is recalled that the present simulation does not include the base flow behind the vehicle. The local interaction

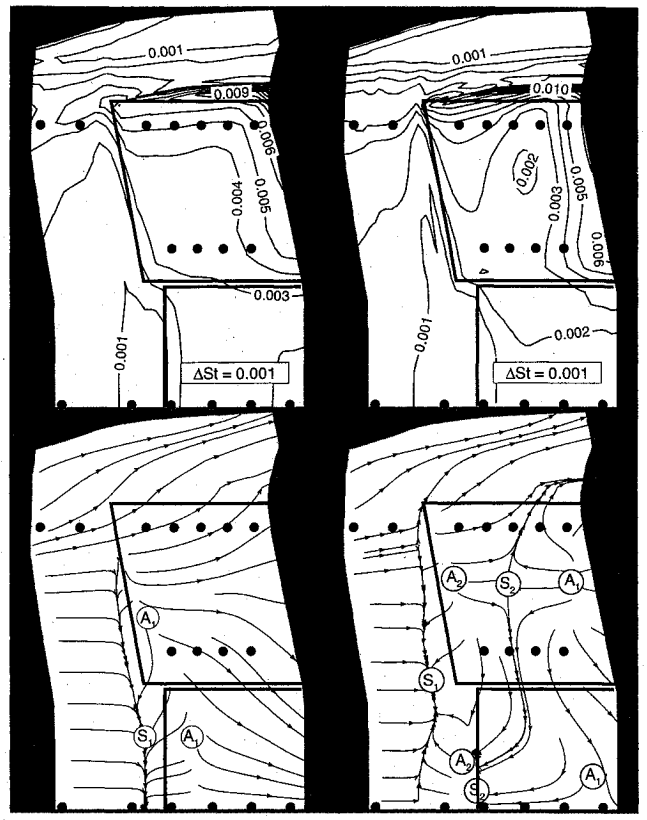

Fig. 7 Computed heat fluxes (top) and streamlines (bottom) for case II; grid sizes: left, 24 × 32 × 24 and right, 48 × 64 × 48.

of the flow expansion behind the trailing edge with the boundary layer just upstream of the edge should be investigated in future.

Figure 7 shows the effects of complete grid refinement on heat fluxes and streamlines for test case II (deflected control surfaces). Based on the results obtained for the clean configuration (case I), the grids used for case II were enriched with more points in crosswise direction by adding 9 grid planes in the region of the external elevon in the fine grid and 5 in the coarse grid. Similar to case I, there is a trend of the heat fluxes to build up two relative maxima at both sides of the elevon trailing edge as the grid is refined. The near-wall streamlines are most sensitive to grid refinement. For both grids the shock induced by the deflection of the control surfaces creates boundary-layer separation along and ahead the elevon and body-flap hinge lines. On the coarse grid, reattachment occurs shortly downstream of the hinge lines. In contrast, the flow reattaches close to the trailing edge on the fine grid. There is a secondary separation bubble embedded in the recirculation flow of the primary separation. The interaction of the primary and secondary bubble shift the primary separation line upstream. Bubble type flows with embedded secondary separation has also been observed on flows over a two-dimensional ramp.[11] The secondary separation is larger on the elevon than on the body flap. This is caused by the additional pressure gradient induced by the concave surface curvature of the elevon. Figure 8 shows line plots of computed heat fluxes for test case II. Because of the multiple flow separations, one can not expect grid independent solutions (also see Refs. 11 and 12). Accordingly, only convergence trends are investigated. Upstream of the primary separation line, good agreement is observed between both solutions. Within the separation zone the discrepancies are larger. The main reason for these discrepancies is the failure of the coarse grid to capture the secondary separation. Finally, Fig. 9 compares the numerical results with the experimental data for case II. In general, good agreement is observed. Only the body flap exhibits significant discrepancies for the region of separated flow. It seems that the wind-tunnel flow is in transition from laminar to turbulent during reattachment, which may also have an effect upon the primary separation line. The transition of the body-flap boundary layer may have some effect on the flow over the elevon, possibly with a reduction

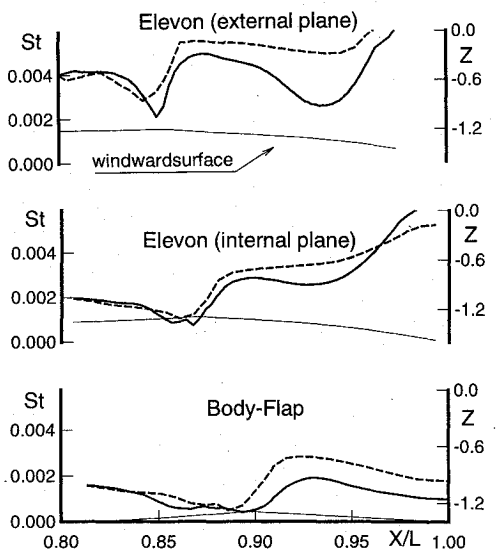

Fig. 8 Line plots of computed Stanton number for case II: ——, fine grid and - - - -, coarse grid.

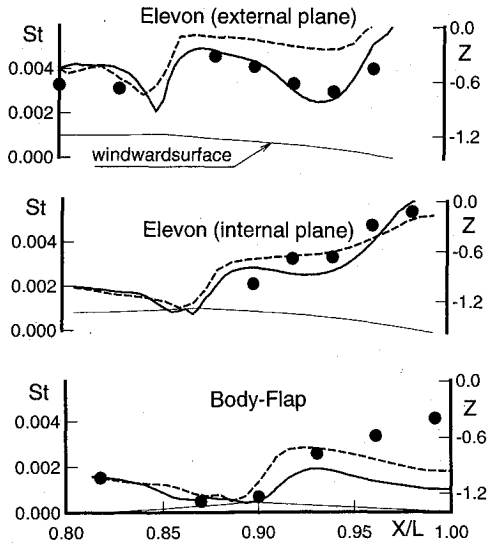

Fig. 9 Line plots of computed and measured Stanton number for case II: ——, fine grid; - - - -, coarse grid; and •, experiments.

of the separation size. For the internal elevon plane, however, the discrepancies between numerical and experimental results are not much larger than two times the experimental accuracy. The good agreement at the external elevon plane indicates that the resulting flow topology in the experiment is similar to that of the fine grid results. Presently there is no explanation for the discrepancies at the external elevon plane ahead of the separation.

Grid convergence studies are also carried out for the flow condition corresponding to a flight trajectory point. The numerical results are obtained on the same grid used for case II. Since high-temperature effects cannot be fully simulated in ground-based facilities at the present, the discussion is based only on numerical results. Figure 10 shows the effects of complete grid refinement on the heat fluxes and resulting streamlines for test case IV (deflected control surfaces). Again, peak heat fluxes are better resolved at both sides of the elevon with increasing grid density. The streamlines show no flow separation on the coarse grid. Incipient flow separation at the hinge lines is observed on the fine grid. Both grids seem to indicate a quasi-two-dimensional flow over the control surfaces with some flow divergence at both elevon sides. Figure 11 shows line plots of computed heat fluxes on selected planes. Quite good agreement is observed between results from both grids because the flow topologies are very similar. For all of the planes, almost grid-independent solutions are achieved.

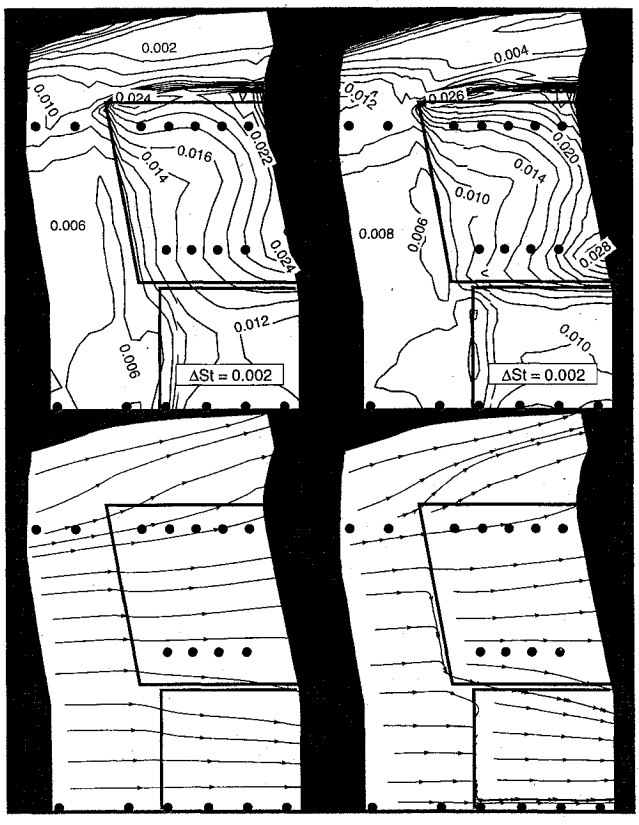

Fig. 10 Computed heat fluxes (top) and streamlines (bottom) for case IV; grid sizes: left, 24 × 32 × 24 and right, 48 × 64 × 48.

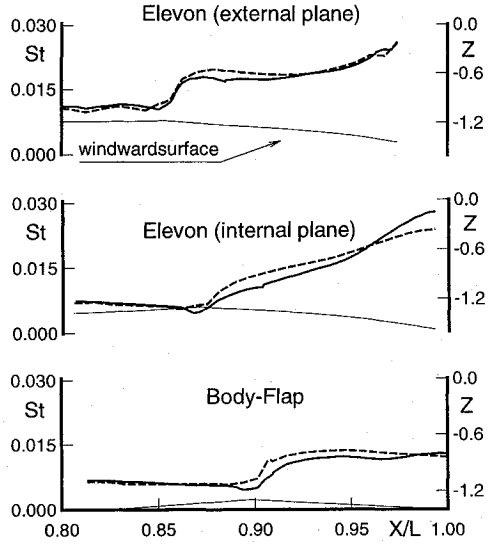

Fig. 11 Line plots of computed Stanton number for case IV: ——, fine grid and - - - -, coarse grid.

Flap Efficiency and Flap Heating

Control surface efficiency and heating are evaluated using cambered and plane geometries in this section. The discussion will be based on fine-grid results. The simulation for the flight case is done assuming flow in thermochemical equilibrium. It is well known that nonequilibrium effects are significant at the flight trajectory point chosen for the present investigation. Recent comparisions[13] of nonequilibrium and equilibrium flows over simplified axisymmetric control surface geometries show that the pressure and heat flux distributions reach their largest values for equilibrium conditions. The results for nonequilibrium flows are in between the perfect gas and equilibrium cases. Hence, one can assume that the use of equilibrium air represents a conservative engineering estimate to make three-dimensional computations, including grid refinement studies and geometry variations, feasible.

Table 2 Computed and measured pitching moment coefficients

Case	Euler $C_{m\delta=0}$	NS[a] $C_{m\delta=0}$	WT[b] $C_{m\delta=0}$	Euler $C_{m\delta=10}$	NS $C_{m\delta=10}$	WT $C_{m\delta=10}$
I	0.0086	0.0083	0.0100	—	—	—
II	—	—	—	−0.0179	−0.0172	−0.0142
III	0.0132	0.0116	—	—	—	—
IV	—	—	—	−0.0222	−0.0236	—
V	0.0117	0.0115	—	—	—	—
VI	—	—	—	−0.0118	−0.0116	—
VII	0.0164	0.0151	—	—	—	—
VIII	—	—	—	−0.0126	−0.0136	—

[a]Navier–Stokes. [b]Wind tunnel.

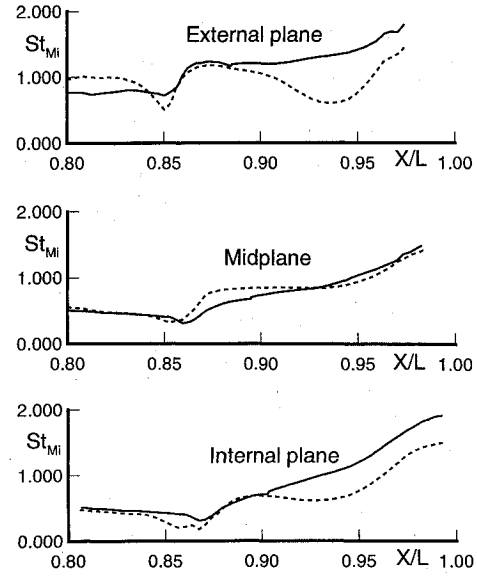

Fig. 12 Line plots of computed Stanton–Miller number for cases II and IV: ——, case IV and - - - -, case II.

Cambered Elevon

Table 2 contains computed and measured values of the pitching moment for all configurations tested. The values obtained by the solution of the Euler equations represent the ideal case where no viscous losses are present. For conditions corresponding to the cold wind tunnel, the viscous effect of the longitudinal aerodynamics characteristic for the clean configuration (attached flow) is a small reduction in nose-up pitching moment. For the configuration with deflected body flap and elevon (multiple flow separations at the control surfaces), the reduction in pitching moment because of viscous effects is similarly small. The wind-tunnel data show higher pitch-up values that may be partially explained by the differences between the geometries of the models used for the numerical and experimental simulations. Nevertheless, there is only 5% difference between computed and measured control surface efficiencies.

The computed viscous control surface efficiency compares quite well with that obtained by the solution of the Euler equations at the flight trajectory point. The viscous value is only marginally smaller, 0.5%, than the result for the inviscid case. The comparison of the pitching moment for the clean configuration obtained at $M_\infty = 25$ and at $M_\infty = 10$ shows a significant increment in pitch-up for the higher Mach number because of the high-temperature effect that yields a larger flow expansion downstream of the stagnation region compared to the perfect gas case. Accordingly, the surface pressures at the body rear are lower that yield a nose-up increment for the clean configuration. The effect is known as pitching moment anomaly in the history of the U.S. Space Shuttle Orbiter development.[2,3,14] Furthermore, the control surface efficiency is 38% larger for flight conditions than for wind-tunnel conditions. Elevon heating for cold wind tunnel and flight conditions (test cases II and IV) is compared in Fig. 12. Even though the flow divergence of the boundary layer

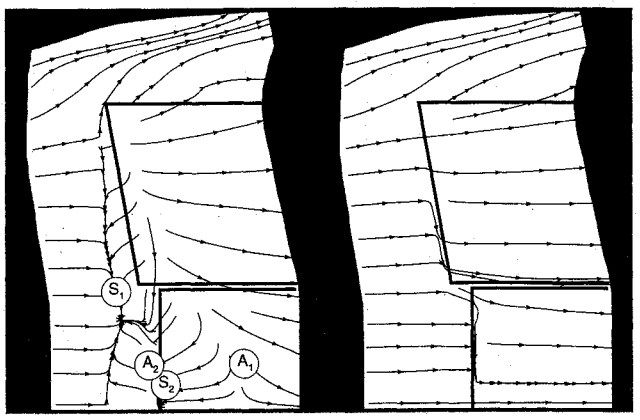

Fig. 13 Computed streamlines for cases VI and VIII.

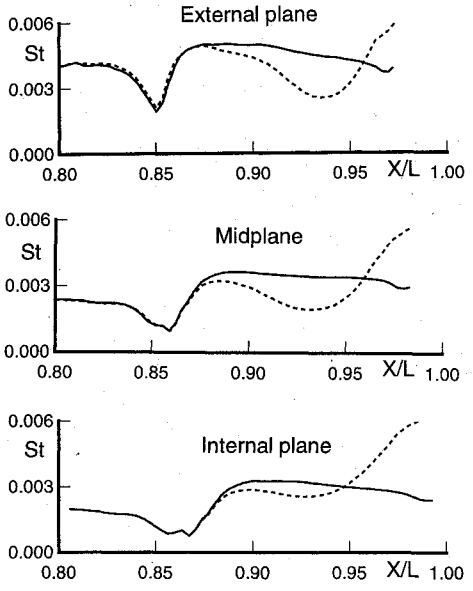

Fig. 14 Line plots of computed Stanton number for case VI: ——, plain and - - - -, cambered.

along the elevon does not seem very noticeable at flight conditions, the heat fluxes show strong peaks at the lateral sides, with local values exceeding about 50% the values found at midspan. This results renders the use of quasi-two-dimensional approaches for engineering heat flux evaluations rather questionable.

Plane Elevon

Figure 13 shows the computed streamlines along the Hermes configuration with plane elevons for test cases VI and VIII (deflected control surfaces $M_\infty = 10$ and 25). In comparison with the cambered elevon, the plane elevon exhibits a strongly reduced separation area at wind-tunnel conditions. At flight conditions, the plane elevon shows a quasi-two-dimensional flow structure. Figures 14 and 15 compare line plots of Stanton number for both elevon geometries and freestream conditions. In all of the cases, the plane elevon displays a plateau shape for the heat fluxes. The low heating rate of the cambered elevon at $X/L \approx 0.93$ (wind-tunnel conditions) is caused by the secondary separation. The heating rate at the trailing edge of the plane elevon, however, is about 50% of the cambered elevon value. This observation is valid for both freestream conditions. It is noted that the local inclination angle of the cambered elevon rear is larger than for the plane. Hence, one expects less control surface efficiency for the plane elevon, which is confirmed by Table 2. The final question is then whether the larger efficiency of the cambered elevon outweighs its heat flux penalties. This is answered by Fig. 16, which shows the peak heating in the midplane of both elevon geometries vs the increment of pitching moment $(C_m - C_{m0})$. The reference condition for heating St_0 is taken at the trailing edge of the control surface for the clean configuration with plane elevons.

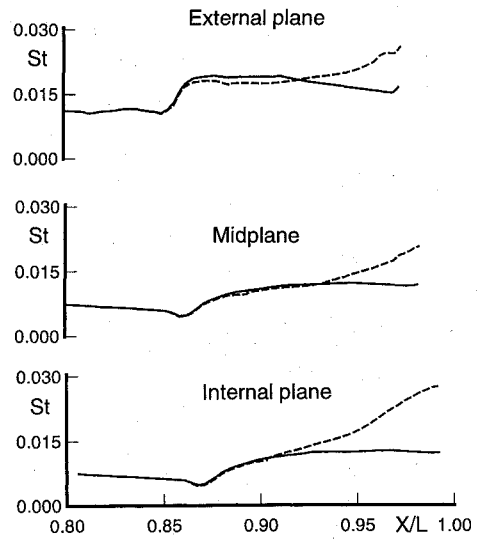

Fig. 15 Line plots of computed Stanton number for case VIII: ——, plain and - - - -, cambered.

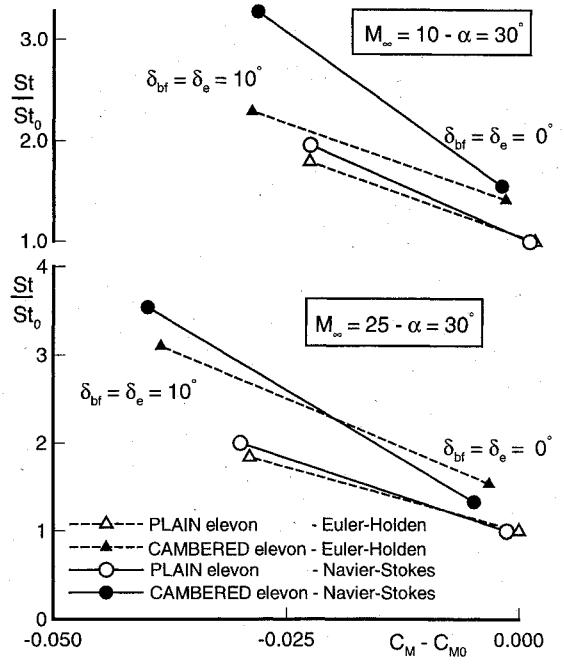

Fig. 16 Elevon peak heating for different freestream conditions and geometries, as a function of the control surface efficiency on pitching moment.

The reference condition for the pitching moment C_{m0} is given by the clean configuration with plane elevons. Under the assumption of a linear variation of maximum heat fluxes for control deflections between $\delta = 0$ and 10 deg, the plane elevon configuration yields lower heating values for given values of $(C_m - C_{m0})$. It is concluded that the present degree of elevon cambering is probably too large for control surface deflection angles $\delta \leq 10$ deg. The loss of control efficiency due to reduced elevon camber could be compensated by cambering the body flap as well. Finally, Fig. 16 is a demonstration that semiempirical estimates of the heat flux based on Euler pressure distributions and correlations for two-dimensional ramp flows[15] are not useful for cambered control surface geometries.

Conclusions

In the present study Navier–Stokes solutions have been analyzed for the European RV Hermes at freestream conditions corresponding to cold wind-tunnel tests at $M_\infty = 10$ and a flight trajectory point at $M_\infty = 25$. The RV is equipped with body flap and elevons as control surfaces. Computations have been carried out for clean configurations and for configurations with deflected control surfaces.

The accuracy of the computed solutions has been addressed by grid refinement studies and by comparing the numerical results with available experimental data. The importance of the viscous effects for the prediction of the pitching moment has been investigated by comparing Navier–Stokes solutions with Euler solutions. Furthermore, the effect of the elevon camber with respect to efficiency and heating has been studied.

The grid convergence study shows grid converged solutions for attached flow, whereas the size of flow separations still depends on grid density. The computed local distributions of wall heat fluxes are in good agreement with measured data for wind-tunnel case. The remaining discrepancies should be investigated by future flow simulations including the effects of the base flow and laminar/turbulent transition.

There is a significant reduction of flow separation if flow conditions are varied from wind tunnel to flight. Also, the present results reveal important three-dimensional effects on elevon heating. These are traced to flow divergence at the lateral edges of the cambered elevon and they are larger for $M_\infty = 25$ than for wind-tunnel conditions.

Finally, the comparison of Euler and Navier–Stokes results indicates that viscous effects on pitching moment and flap efficiency are rather small for Hermes at the chosen trajectory point.

Acknowledgment

The present investigations were partially funded under Contract ESA-CNES 9628-91-F-BM, DLR Technical Assistance to Centre National d'Etudes Spatiales (CNES) concerning Hermes Aerothermodynamics and monitored by G. Durand, CNES-Toulouse, France.

References

[1]Isakeit, D., "High Temperature Aspects of the European Hermes Programs," *3rd Aerospace Symposium*, edited by H. Oertel and H. Körner, Springer–Verlag, Braunschweig, Germany, 1991, pp. 83–102.

[2]Bertin, J. J., "Defining the Shuttle Pitching Moment—A Historical Review," *Hypersonic Aerothermodynamics*, edited by J. S. Przemieniecki, AIAA Education Series, AIAA, Washington, DC, 1994, pp. 141–143.

[3]Maus, J. R., Griffith, B. J., Szema, K. Y., and Best, J. T., "Hypersonic Mach Number and Real Gas Effects on Space Shuttle Orbiter Aerodynamics," AIAA Paper 83-0343, Jan. 1983.

[4]Weilmuenster, K. J., Gnoffo, P. A., and Greene, F. A., "Navier–Stokes Simulations of the Shuttle Orbiter Aerodynamic Characteristics with Emphasis on Pitch Trim and Body Flap," AIAA Paper 93-2814, July 1993.

[5]Kroll, N., Radespiel, R., and Rossow, C.-C., "Accurate and Efficient Flow Solvers for 3D Applications on Structured Meshes," AGARD Fluid Dynamics Panel, Special Course on Parallel Computing in CFD, 1995, pp. 4.1–4.59 (AGARD-R-807).

[6]Stojanowski, M., "Hermes 1.0—Mesure des flux thermiques avec thermocouples sur la maquette no. 3041 au 1/40 dans la soufflerie S4MA a Mach 10," Dassault Aviation, AMD-H.RE.1.1114, Velizy, France, Nov. 1992.

[7]Stojanowski, M., "Hermes 1.0 au 1/40 a S4MA—Identification aérodynamique a Mach 10 avec la maquette no. 3026," Dassault Aviation, AMD-H.RE. 1.1106, Velizy, France, June 1992.

[8]Porier, D., Findling, A., and Radespiel, R., "Longitudinal Control Efficiency of Hermes (1.0) with Straight Elevons at High Mach Numbers," Deutsche Forschungsanstalt für Luft- und Raumfahrt e.V., DLR-IB-129-91/28, Braunschweig, Germany, Aug. 1991.

[9]Herrmann, U., Radespiel, R., and Longo, J. M. A., "Critical Flow Phenomena on the Winglet of Winged Reentry Vehicles," AIAA Paper 94-0629, Jan. 1994.

[10]Herrmann, U., and Porier, D., "Interpolation Procedure Allowing Local 3D Navier–Stokes Computations on Refined Meshes," Deutsche Forschungsanstalt für Luft- und Raumfahrt e.V., DLR-IB-129-93/5, Braunschweig, Germany, May 1993.

[11]Abgrall, R., Désidéri, J., Mallet, M., Périaux, J., Perrier, P., and Stoufflet, B., "Synthesis of the Workshop on Hypersonic Flows for Reentry Problem," *AGARD Fluid Dynamic Panel Symposium on Theoretical and Experimental Methods in Hypersonic Flows*, AGARD-CP-514, Torino, Italy, 1992, pp. 18-1–18-23.

[12]Longo, J. M. A., and Nickel, H., "Flow Simulation Around HALIS Configuration at Wind Tunnel Conditions," *Proceedings of the 4th European High-Velocity Database Workshop*, ESA, ESTEC Noordwijk, The Netherlands (to be published); also DLR-IB 129-94/27, 1995.

[13]Brenner, G., "Numerische Simulation von Stoß-Stoß und Stoß-Grenzschichtwechselwirkungen in reagierenden Hyperschallströmungen," *Arbeitsgemeinschaft Strömungen mit Ablösung (AG STAB)*, Jahresbericht 1992, DLR, Göttingen, Germany, 1993, pp. 191, 192.

[14]Brauckmann, G. J., Paulson, J. W., Jr., and Weilmuenster, K. J., "Experimental and Computational Analysis of the Space Shuttle Orbiter Hypersonic Pitch-Up Anomaly," AIAA Paper 94-0632, Jan. 1994.

[15]Holden, M. S., "A Review of Aerothermal Problems Associated with Hypersonic Flight," AIAA Paper 86-0267, Jan. 1986.

K. J. Weilmuenster
Associate Editor